npj | flexible electronics

Article

Published in partnership with Nanjing Tech University

https://doi.org/10.1038/s41528-026-00617-6

Graded-modulus tri-layer substrates for stress-relieved direct fabrication of integrated stretchable systems

Check for updates

Shusuke Yamakoshi[1], Fumika Nakamura[1], Sho Sato[1], Yuji Isano[1], Yutaka Isoda[2], Tamami Takano[2], Kyohei Nagatake[1], Ryosuke Matsuda[1], Naoko Namba[3], Tsuyoshi Sekitani[3,4], Takafumi Uemura[3,5] ✉ & Hiroki Ota[1,2,6] ✉

Stretchable electronics capable of integrating high-performance components while accommodating large mechanical deformations are increasingly in demand for wearable devices and soft robotics. Conventional substrates composed solely of soft materials exhibit limited mechanical and thermal tolerances for thin-film processing, whereas hybrid structures combining soft and rigid substrates exhibit severe interfacial stress and delamination caused by the large difference in Young's modulus between the materials. This study proposes a tri-layer hybrid substrate made of Ecoflex, polydimethylsiloxane, and epoxy resin with graded Young's moduli, which effectively relaxes the interfacial stress while maintaining mechanical and thermal stability. It withstands up to 300% tensile strain and enables the direct deposition of organic thin-film transistors and incorporation of integrated circuit components without any transfer process. This study presents a versatile platform capable of directly integrating rigid and thin-film electronic devices on a single substrate, thus paving the way for highly integrated and practical stretchable electronic systems.

In recent years, stretchable electronics have been actively researched for applications in advanced wearable devices and soft robotics. Numerous studies have reported stretchable electronic devices capable of detecting physical quantities such as strain[1–3], temperature[4], and pressure[5]. These devices utilize carbon nanostructures[1], metal nanostructures[2], ion gels[3], and hydrogels[4,5] in combination with highly stretchable rubber materials[1,2,4] or gel materials[3,5].

Currently, stretchable devices, wherein not only the individual components but the entire system is stretchable, are being explored for realizing highly functional and high-performance devices[6–9]. Two main approaches have been adopted to realize such devices. The first approach involves fabricating all components, including electronic components, using stretchable materials[10–12]. However, this method relies strongly on the material properties, limiting the types of elemental materials that can be used. Consequently, this method has limitations related to the variety and performance of sensors and transistors[13–15], thus presenting a significant challenge for multimodal sensing and circuit integration.

The second approach utilizes soft–rigid stretchable electronic (SRSE) substrates that seamlessly combine rigidity and flexibility[16–18]. In stretchable electronics, devices that use SRSE substrates are called stretchable hybrid devices, where a rigid region is incorporated on a stretchable substrate to enable the placement of rigid circuit components. Stretchable hybrid devices are realized through several techniques, such as placing a supporting platform on the substrate to secure the components and prevent failure during stretching[16], surrounding the device with a flexible substrate[17], using two types of silicone resins with different Young's moduli[18], engineering the interfacial transition between rigid and stretchable regions through bioinspired mechanical interlocking structure[19,20], and spatially controlling the crosslink density of the substrate to form strain-engineered modulus gradients[21]. By utilizing SRSE substrates, conventional solid-state electronic components and surface-mounted device (SMD)-type integrated circuit (IC) chips can be directly mounted onto a rigid region[16–22]. In addition, it offers the advantage of ensuring the overall stretchability of the system while maintaining its compatibility with existing high-performance components.

SRSE substrates utilize materials that combine flexible substrates with rigid silicone resins such as PDMS-Ecoflex[18], PI-Ecoflex[19,20], PLA-Ecoflex[23], and SU-8-PDMS[24,25]. These materials enable mounting of solid device sections while maintaining the overall stretchability of the device. Mounting

[1]Department of Mechanical Engineering, Yokohama National University, Yokohama, Kanagawa, Japan. [2]Graduate School of System Integration, Yokohama National University, Yokohama, Kanagawa, Japan. [3]SANKEN (The Institute of Scientific and Industrial Research), The University of Osaka, Ibaraki, Osaka, Japan. [4]Graduate School of Engineering, The University of Osaka, Suita, Osaka, Japan. [5]Graduate School of Information Science and Technology, The University of Osaka, Suita, Osaka, Japan. [6]Institute of Advanced Sciences, Yokohama National University, Yokohama, Kanagawa, Japan.
✉e-mail: uemura-t@sanken.osaka-u.ac.jp; ota-hiroki-xm@ynu.ac.jp

solid devices, such as IC chips, is relatively easy, but the direct application of thin-film processing techniques is difficult. High-precision mounting of thin-film devices, such as thin-film transistors (TFTs) and organic thin-film transistors (OTFTs), has depended on indirect methods involving transfer from a rigid substrate to a stretchable substrate or stretchable hybrid substrate[26]. Incorporating thin-film devices using these indirect methods is challenging for high-density integration because of positional accuracy issues and the risk of device damage[27]. Direct application of the thin-film processing technology is essential for the high-density patterning of thin-film devices on flexible substrates. However, this technology requires a rigid substrate surface that resists deformation at high temperatures and exhibits strong chemical resistance.

Materials such as PLA, SU-8, and epoxy resin exist as hard layers that satisfy these conditions. However, a large disparity in Young's modulus exists at the boundary between the soft and rigid layers. This significant difference in modulus can cause stress concentration, potentially severely compromising durability during device stretching. Therefore, for scalable stretchable electronics, it is important to develop SRSE substrates comprising a thermally and chemically resistant hard layer and a soft layer capable of large deformations to enable the mounting of both solid-state and thin-film devices using existing fabrication methods.

The interconnect material is another critical factor for stretchable hybrid devices, as it must balance both electrical conductivity and mechanical compliance under repeated deformation. Stretchable wiring approaches are broadly divided into structural techniques—including wrinkle[28], island-bridge[29], origami[30], fiber-mesh[31], and kirigami geometries[32] that mechanically accommodate strain—and material-based techniques that rely on intrinsically stretchable conductors such as carbon[33], PEDOT:PSS[34], silver paste[35], and liquid metals (LMs)[36]. Structural approaches achieve excellent resistance stability but require additional spatial footprint that limits high-density integration. In material-based techniques, commonly used conductors exhibit limitations: carbon suffers from low conductivity[37], PEDOT:PSS requires hydrogel or ion-gel networks whose long-term stability is limited[34], and silver paste exhibits abrupt resistance changes under strain due to percolation behavior[38]. Gallium-based LMs, in contrast, combine metallic conductivity with the continuity and deformability of a liquid, offering stable resistance under repeated deformation. Accordingly, they have become particularly attractive—though not exclusive—as interconnects in stretchable hybrid integration[39].

In this study, an SRSE substrate was developed using three materials with different Young's moduli. This SRSE substrate enables the mounting of solid-state devices, such as ICs, and the direct patterning of thin-film electronic devices using existing thin-film processing methods. This substrate comprises a thermally and chemically resistant epoxy resin as a rigid layer, PDMS as a middle layer to mitigate the abrupt change in the Young's modulus between the rigid and soft layers, and Ecoflex as a soft layer to achieve a large deformation. A stretchable temperature sensor using multiple rigid elements, a stretchable logic circuit, and a stretchable active matrix fabricated using TFTs was used to demonstrate the proposed substrate. Because thin films can be directly laminated onto substrates, not only various rigid ICs but also thin-film electronic devices can be mounted on this substrate. While our previous report addressed only the localized reinforcement of junctions between LM interconnects and rigid circuits on planar polyimide substrates, the present work redesigns the entire rigid–soft composite substrate, providing arbitrarily shaped, deposition-compatible rigid islands together with a robust adhesive-free interfacial architecture that withstands strains beyond 300%. This is a fundamental technology that will contribute to advancing the applications of stretchable hybrid devices.

Results

Structure of SRSE Substrate

The SRSE substrate is composed of three materials with different Young's moduli—Ecoflex as the soft layer, PDMS as the middle layer, and epoxy resin as the rigid layer. This design enables the direct mounting of ICs and direct fabrication of thin-film electronic devices such as TFTs and OTFTs, thus conferring versatility and multifunctionality to stretchable hybrid devices (Fig. 1a). The electronic components, such as ICs, TFTs, and OTFTs, are implemented on the rigid layer, and the wiring between the electronic components is fabricated using an LM paste. The LM paste wiring is used to create a stretchable circuit, which is then encapsulated within the rigid, middle, and soft layers of the substrate. The stretchable hybrid device fabricated using the above design exhibits both high stretchability and functionality.

The key feature of this substrate is its ability to support direct mounting of rigid electronic components, such as SMD-type components, and fabrication of thin-film components, such as TFTs and OTFTs, via direct deposition and sputtering. The soft layer fabricated using Ecoflex00-50 has a Young's modulus comparable to that of human skin, providing flexibility and stretchability. The epoxy resin used in the rigid layer is thermally and chemically resistant with a high Young's modulus. The PDMS used in the middle layer bridges the gap in the Young's modulus of the rigid and soft layers. The proposed structure enables the prevention of stress concentration owing to the gap between the rigid and soft layers to realize large stretchability (Fig. 1b). Direct mounting of electronic components and fabrication of thin-film components require a planar rigid layer. In this study, epoxy resin was formed into a flat surface using an interface treatment. The material composition of the substrate and optimization of the hard layer support the direct mounting of solid-state components and direct fabrication of thin-film components on the SRSE substrate.

In this study, solid-state devices were mounted on the fabricated SRSE substrates by die mounting, and OTFTs were fabricated using direct standard vapor deposition (Fig. 1c). The fabricated OTFTs were top-contact bottom-gate type devices that used Dinaphtho[2,3-*b*:2',3'-*f*] thieno[3,2-*b*] thiophene (DNTT) as the semiconductor layer and parylene as the insulating layer. LM wiring was applied between the components. The wiring intersection points were insulated using Ecoflex 00-50. Additional LM wiring was screen-printed using the same method after curing. Devices fabricated using this method exhibit stretchability, which enables them to withstand stretching and bending. To demonstrate stretchable hybrid devices, stretchable standalone temperature sensors incorporating rigid components, stretchable logic circuits based on OTFTs, and multipixel active matrices based on OTFTs have been developed.

Fabrication process of SRSE substrate

A key contribution of this study is the development of a tailored fabrication process for the SRSE substrate, as shown in Fig. 2. First, a substrate with a convex dome-shaped pattern was fabricated using a 3D printer. PDMS was applied as the middle layer and cured on top of the substrate (Fig. 2(i)). Ecoflex 00-50 as the soft layer was coated using a spin coater and cured (Fig. 2(ii)). This substrate was then laminated with a PEN (polyethylene naphthalate) film coated with PVA (polyvinyl alcohol) and released from the 3D-printed mold (Fig. 2(iii)). The PI (polyimide) mask was placed on the substrate surface as a mask for excimer treatment; this was performed only on the PDMS layer to activate its surface (Fig. 2(iv)). Epoxy resin as the rigid layer was screen-printed on the PI mask, after which the mask was removed and cured (Fig. 2(v)). Electronic components were placed on the epoxy resin, and LM wiring was screen-printed (Fig. 2(vi)). The epoxy resin, PDMS, and Ecoflex 00-50 were sequentially encapsulated from the top (Fig. 2(vii)). The sacrificial PVA layer was dissolved in pure water and peeled off from the PEN film to fabricate the stretchable hybrid device on the SRSE substrate (Fig. 2(viii)).

Mechanical characterization of SRSE substrate

The Young's modulus values and tensile stress–strain curves for all three materials comprising the modulus-gradient structure are summarized in Supplementary Figure 1 and Supplementary Table 1. Test specimens were fabricated at film thicknesses close to those used in the actual device. The stiffness ratio between the soft layer (Ecoflex 00-50, 114 kPa) and the intermediate layer (PDMS, 651 kPa) is approximately five times, while the ratio between the intermediate and rigid layers (epoxy resin, 1.75 GPa) is

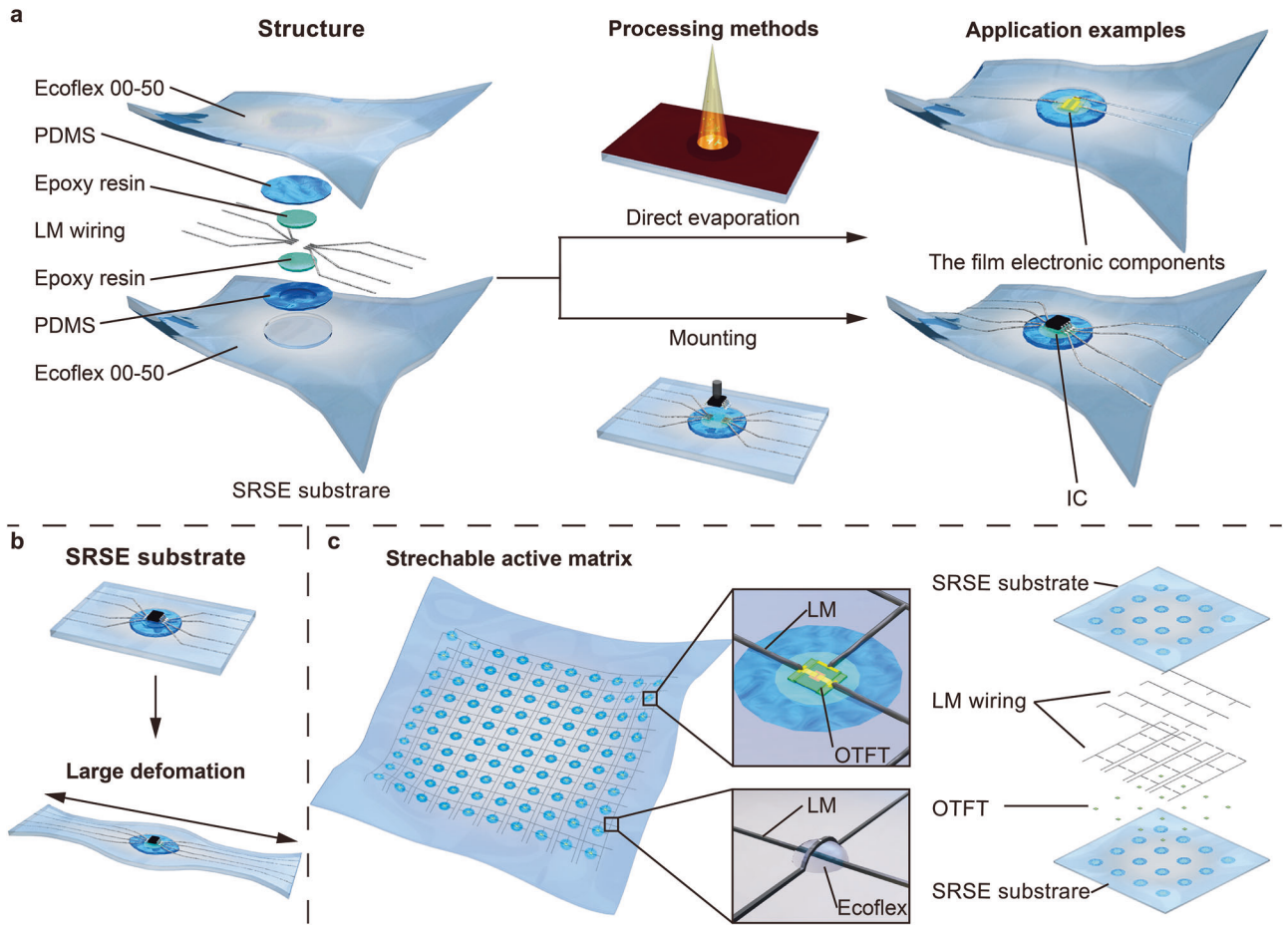


Fig. 1 | Highly stretchable and functional SRSE substrate. a The substrate has a three-layer structure. The soft layer comprises Ecoflex00-50, the middle layer comprises PDMS, and hard layer comprises epoxy resin. LM paste wiring, vapor deposition, and die mounting were performed on the SRSE substrate to mount the OTFTs and ICs. **b** The fabricated substrate has three layers to prevent rapid changes in the Young's modulus and is highly stretchable. **c** OTFTs can be freely fabricated on this SRSE substrate using conventional thin-film processing techniques, such as vapor deposition. This enables the realization of a stretchable active matrix.

approximately 2700 times, yielding an overall soft-to-rigid stiffness ratio of approximately 15,000 times. This graded stiffness profile is achieved through material selection alone, without relying on geometric modulus-gradient designs, thereby offering a significant advantage over existing strategies.

Figure 3a shows the photographs of the entire substrate under 50% tensile strain and the corresponding strain distributions. To evaluate and compare the mechanical properties of the fabricated substrates, three types of substrates were prepared: (i) a two-layer substrate composed of soft and rigid layers, (ii) a two-layer substrate composed of soft and middle layers, and (iii) a three-layer substrate composed of soft, middle, and rigid layers.

To make the individual layers easily distinguishable, the rigid layer is shown in black, and the middle layer is shown in red. The graphs in Fig. 3b show the strain values as a function of the distance from the center of the substrate. Fig. 3a(i) and b show that the substrate composed of only soft and middle layers was significantly stretched in the central region. In contrast, Fig. 3a(ii), (iii) show that the two-layer substrate composed of soft and rigid layers and the three-layer substrate composed of soft, middle, and rigid layers had areas that remained almost strain-free. However, the two-layer substrate comprising soft and rigid layers had few regions that mitigated the displacement and exhibited the smallest strain at break among the three types of substrates (Fig. 3c). This result is consistent with previous reports showing that joining materials with large differences in Young's moduli leads to high localized stresses, making them easier to break[40]. The adhesion at the PDMS–Ecoflex interface and its potential influence on device reliability were also examined. Prior studies have established a robust bond between PDMS and Ecoflex, reporting that directly bonded specimens result in bulk Ecoflex fracture rather than interfacial delamination even under large tensile deformation[41,42]. Consistent with these reports, the stress–strain curve of the Ecoflex–PDMS two-layer substrate (Fig. 3c) confirms that it withstands tensile strains exceeding 300%. Furthermore, to verify the mechanical performance of the proposed soft–rigid composite structure across a wide strain range, DIC analysis was performed on the three-layer substrate at tensile strains of 50%, 100%, 150%, 200%, 250%, and 300% (Supplementary Figure 2). At low-to-moderate strains (50–100%), a stable low-strain region was consistently observed at the device center, confirming that the applied deformation is primarily absorbed by the soft layer while the intermediate and rigid layers remain effectively protected from mechanical deformation. At higher strains (150–300%), the strain begins to propagate into the intermediate layer; however, deformation at the rigid layer remains suppressed, demonstrating that the proposed three-layer modulus-gradient structure continues to function effectively even under large deformations. No failure was observed at the Ecoflex–PDMS interface under any of the tested conditions; in contrast, the strain concentration near the PDMS–epoxy interface increased above 150% strain, and fracture initiation occurred above 300% strain. These results confirm that the proposed three-layer structure maintains its stress-relieving function up to 300% strain, and that the PDMS–epoxy interface represents the primary reliability boundary of the present device.

The surface structure of the epoxy resin was examined by fixing the diameter of the bottom surface of the convex dome-shaped spherical recess on the patterned substrate at 6 mm and varying the curvature radius. Fig. 3d

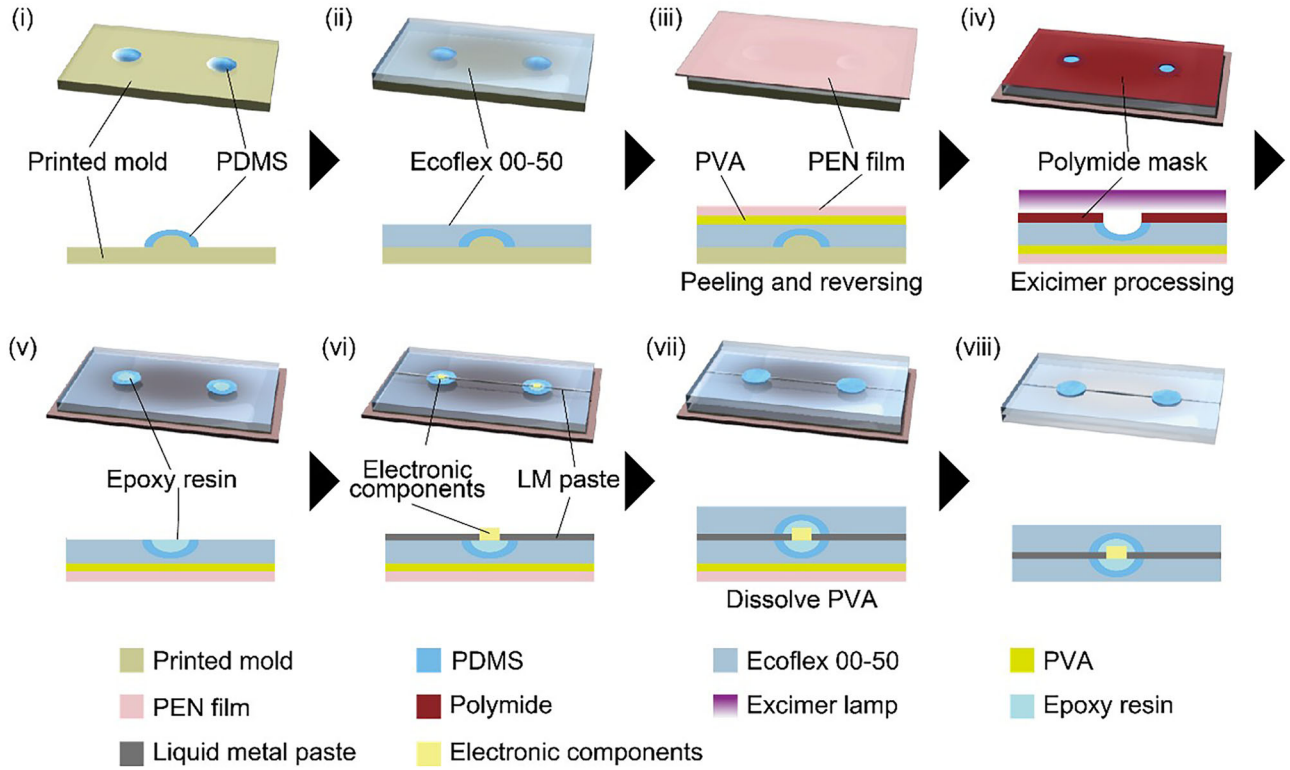


Fig. 2 | Fabrication process of the SRSE substrate. (i) PDMS is applied as the middle layer and cured on top of the 3D-printed substrate. (ii) Ecoflex 00-50 is coated as the soft layer using a spin coater and cured. (iii) This substrate is laminated with a PEN film coated with PVA and released from a 3D-printed mold. (iv) A PI mask is placed on the substrate surface for excimer treatment, which is performed using only the PDMS layer to activate its surface. (v) The epoxy resin as the rigid layer is screen-printed onto the PI mask, after which the mask is removed and cured. (vi) Electronic components are placed on the epoxy resin, and LM wiring is screen-printed. (vii) The epoxy resin, PDMS, and Ecoflex 00-50 are sequentially encapsulated from the top. (viii) The sacrificial PVA layer is dissolved in pure water, and the PEN film is peeled off to fabricate a stretchable hybrid device on the SRSE substrate.

shows the distance x from the edge of the epoxy resin and the displacement y relative to the edge. The graph shows that the center of the epoxy resin surface tends to bulge as the radius of curvature decreases, and the pattern shape becomes increasingly rounded. However, as the radius of curvature increases, that is, as the shape approaches flatness, the central region of the epoxy resin surface forms a concave structure.

Epoxy resins exhibit low adhesion to silicone resins such as PDMS, making direct bonding generally difficult. In this study, as the middle layer was composed of PDMS and the rigid layer was composed of epoxy resin, the PDMS surface was irradiated with plasma light to improve its wettability and enhance adhesion to epoxy resin[43,44]. Further, excimer treatment was applied to the concave mold structure formed by PDMS, enabling bonding with epoxy resin while allowing flexible patterning of the epoxy layer geometry. However, achieving a smooth epoxy resin surface with the proposed structure requires careful optimization. When the PDMS layer has a small radius of curvature and the pattern is rounded, it forms sides and curved surfaces that cannot be activated by plasma irradiation, hindering sufficient improvement in wettability. Consequently, the surface of the epoxy resin tends to become rounded. In contrast, patterns with a large curvature radius exhibit a nearly flat surface, which is sufficiently activated by plasma irradiation. The improved wettability causes the epoxy resin to spread more readily, resulting in greater resin accumulation and increased thickness at the center. As the thicker central portion undergoes greater shrinkage during thermal curing[45,46], the central area becomes indented. Based on these observations, the curvature radius was systematically varied to identify the optimal value that avoids both central indentation and edge rounding. Consequently, a curvature radius of R22.5 mm yielded the best surface planarity for a rigid layer diameter of 6 mm; accordingly, this value was adopted for device fabrication.

When thin-film electric components are fabricated using vapor deposition, fine patterns are formed by the masks, which are stacked across multiple layers. Previous research has reported that pentacene TFTs fabricated via a SiO_2 layer deposition on a glass substrate exhibited an eightfold increase in mobility when the channel width was reduced relative to the channel length[47]. This suggests that the channel geometry and patterning precision can significantly affect the performance of TFTs and OTFTs. To achieve precise patterning, it is essential to maintain the planarity of the epoxy resin surface. However, the optimal values for various parameters may differ depending on the desired size of the rigid layer. Therefore, further investigation into the effects of shape variations is essential.

The actual diameters of the epoxy layers, relative to their design values, are shown in Fig. 3e. Fifteen samples were fabricated, and their diameters were measured. Fig. 3e shows that the process used in this study can deposit epoxy layers with diameters ranging from 2–10 mm. The minimum diameter of 2 mm corresponds to a size of approximately 4 mm^2, comparable to that of a typical IC (SOT-23: ~3.8 mm^2), suggesting a sufficient integration density for IC implementation. In contrast, configurations with 347 stretchable transistors per 1 cm^2 have been achieved in recent studies on stretchable OTFT devices[48]. Designs enabling higher integration are desired for the fabricated SRSE substrates. Fig. 3f shows the rigid layer on the SRSE substrate, fabricated in a circular shape with diameters of 2 mm, 4 mm, and 6 mm, as well as in triangular and star shapes. This result confirms that both the diameter and shape exhibit a high degree of tunability in this method. Therefore, the rigid layer, which acts as a device protection layer, can be in any desired shape depending on the application. Although the substrates presented here have limited integration density for TFT and OTFT applications, further optimization of the fabrication process, such as improved patterning precision, could enable a higher level of integration in the future.

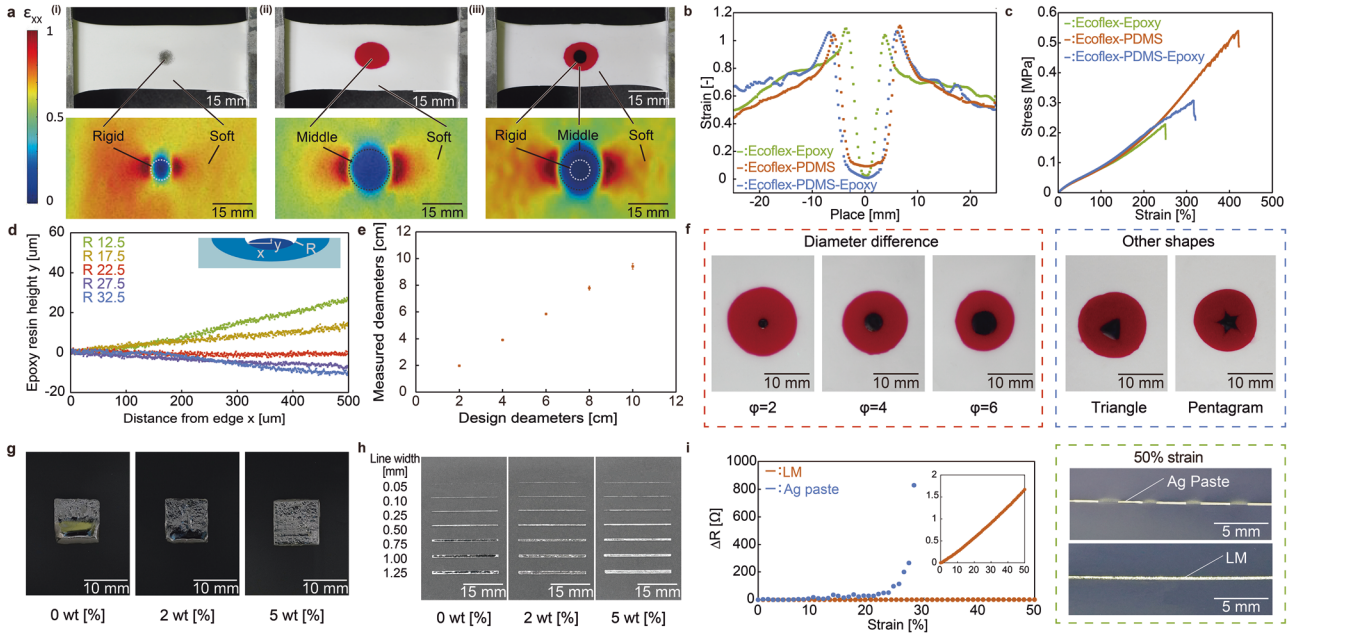


Fig. 3 | Characterization of the SRSE substrate and LM wiring. a Photographs of the entire substrate under 50% tensile strain and the corresponding strain distribution obtained by digital image correlation (DIC). (i) Two-layer substrate composed of a soft layer and rigid layer (Ecoflex–epoxy). (ii) Two-layer substrate composed of a soft layer and intermediate layer (Ecoflex–PDMS). (iii) Three-layer substrate composed of a soft layer, intermediate layer, and rigid layer (Ecoflex–PDMS–epoxy). **b** Strain values as a function of the position from the substrate center. **c** Tensile test results for the Ecoflex–epoxy, Ecoflex–PDMS, and Ecoflex–PDMS–epoxy substrates. **d** Evaluation of the surface profile of the epoxy resin. The x-axis represents the distance from the center, and y-axis represents the height of the epoxy layer. **e** Measured diameters of the epoxy layer relative to their design values. The process can form epoxy layers with diameters of 2–10 mm. **f** Free-form shapes of the epoxy layer. Various geometries of the epoxy layer can be fabricated. **g** Comparison of LM viscosity as a function of the nickel content (0 wt.%, 2 wt.%, 5 wt.%). When LM patterns are formed and placed vertically at 90°, dripping is observed for 0 wt.% and 2 wt.% samples, whereas no dripping occurs for the 5 wt.% sample. **h** LM wirings fabricated using LM with nickel contents of 0 wt.%, 2 wt.%, and 5 wt.%. From top to bottom, line widths of 0.05 mm, 0.10 mm, 0.25 mm, 0.50 mm, 0.75 mm, 1.00 mm, and 1.25 mm are produced. **i** Changes in resistance under tensile deformation for 5 wt.% nickel-containing LM wirings and Ag paste wirings fabricated on Ecoflex 00-50, along with their respective states at 50% tensile strain.

The epoxy layer was given a dome-shaped mold structure to achieve a smooth surface. It was further hypothesized that the dome-shaped geometry would provide additional stress relaxation than a cylindrical geometry at the soft–rigid interface. To verify this hypothesis, finite element method (FEM) simulations were performed using COMSOL Multiphysics for comparing the dome-shaped and cylindrical interface geometries. The experimentally obtained Young's modulus values for epoxy resin (1.75 GPa), PDMS (651 kPa), and Ecoflex 00-50 (114 kPa) were used, with each material modeled as a linear elastic solid. Two interface geometries—dome-shaped and cylindrical—were compared under identical boundary conditions, with one YZ face fixed and a uniaxial tensile strain of 10% applied to the opposite face. The von Mises stress distributions are shown in Supplementary Figure 3 as 3D overviews, XZ cross-sections parallel to the tensile direction, and YZ cross-sections perpendicular to the tensile direction. The XZ and YZ cross-sectional maps show that the cylindrical interface develops a sharp stress concentration band at its upper edge, whereas the dome-shaped interface distributes stress smoothly across the curved surface. Quantitatively, the maximum interfacial stress in the dome geometry is approximately 60% lower than that in the cylindrical geometry, and this trend is consistent across both cross-sectional planes, demonstrating that the stress-relieving effect of the dome shape is three-dimensional and isotropic. These FEM results are in qualitative agreement with the DIC measurements, mechanistically demonstrating that the dome-shaped interface reduces stress concentration at the soft–rigid boundary under a large strain.

In addition, the present study employs a rigid-on-rigid sandwich structure in which the active devices are encapsulated between epoxy resin layers from above and below. To verify that this structure does not introduce excessive localized stress near the encapsulated devices, FEA was performed using the experimentally determined material parameters for Ecoflex, PDMS, and epoxy resin (Supplementary Figure 4). The encapsulated rigid component was modeled as a copper-equivalent material (Young's modulus: 118 GPa). The simulation results show that the maximum von Mises stress near the active device region is approximately 0.60 MPa, which is well below the fracture strength of both the epoxy encapsulant and device substrate materials. The normalized principal strain distribution further confirms that the strain within the epoxy-encapsulated region is effectively zero, indicating that encapsulated devices are largely shielded from externally applied deformation.

Further, the long-term mechanical reliability of the SRSE substrate was evaluated by cyclic tensile testing at 100% strain amplitude for 1500 cycles (Supplementary Figure 5). Initial stress softening attributable to the Mullins effect was observed in the early cycles[49], but the stress–strain behavior converged after approximately 100 cycles and remained stable and reproducible through 1500 cycles, with no significant fatigue degradation observed.

The SRSE substrate fabricated in this study was designed to withstand 300% strain by using epoxy resin with a flat surface and high resistance to external influences around the device periphery and by employing a three-layer structure to reduce localized stress and increase fracture strain. The above results indicate that stress relaxation through multilayering and material selection was effective.

The shape instability of LMs used as wiring materials poses a significant challenge in the practical application of wearable devices. Gallium-based single-phase LMs, such as Galinstan, exhibit extremely low wettability[50], which makes it difficult to achieve high-resolution patterning by screen printing or mask printing. The mechanism underlying this behavior is as follows. Ga-based LMs exhibit an extremely high surface tension at room temperature (548.8 mN/m for Galinstan[50]); therefore, direct application of a single-phase LM readily causes droplet coalescence, making the formation of fine lines in the order of 50 μm difficult. To overcome this challenge, we

employed a two-phase paste in which Ni particles were added to a GaInSn alloy. Through the introduction of Ni particles and subsequent mixing by ultrasonic treatment, the oxidation of gallium is promoted, and the Ni particle surfaces become coated with a Ga oxide film, while gallium oxide is also dispersed throughout the bulk of the LM[51,52]. This internal oxide dispersion maintains the Ni particles in a suspended state, and the mutual support between the two components increases the elastic modulus, yield stress, and viscosity of the LM, transforming it into a gel-like paste[51,52]. Consequently, the LM fills fine gaps via shear-thinning behavior during mask printing, and the enhanced shape-retention capability after dispensing enables the realization of 50 μm-wide ultrafine wiring. It should also be noted that coating methods relying solely on oxide-film accumulation[53] result in a substantial increase in resistivity and were therefore not adopted in this study.

Figure 3g shows the variation in the coating behavior of the LMs with viscosity on Ecoflex 00-50. After the excimer ultraviolet treatment of the substrate, an LM paste with varying concentrations of Ni particles was applied by screen printing. The samples were allowed to stand vertically for one hour after printing. The LM pastes with 0 and 2 wt.% nickel exhibited a downward liquid flow because of gravity. However, no dripping was observed with the 5 wt.% paste. Printing different wiring widths with different paste concentrations revealed that only the 5 wt.% paste successfully formed an uninterrupted 50 μm-wide wiring (Fig. 3h). This result was attributed to the balance between the concentration of conductive particles and viscosity of the paste, which provided the most stable circuit formation during printing. Based on the above results, we adopted 5 wt.% LM paste as the interconnecting material owing to its high operability, stable wiring, and shape stability during deformation.

While the MALMPs system reported by Gul et al. [54] achieves wetting on diverse substrates without pre-treatment, the present study realizes 50 μm-wide ultrafine patterning on elastomeric substrates in a single-step process using LM paste combined with excimer UV treatment. Compared with other LM-patterning approaches, including direct-writing (1.9 μm)[55], NECP (5 μm)[56], EHD printing (<20 μm)[39], and femtosecond-laser patterning (<50 μm)[57], photolithography-based methods (5 μm)[58], mask and screen printing generally produce feature sizes of 20–200 μm[59,60]. This study achieved 50 μm stretchable wiring through the superior shape-retention of the LM paste and excimer surface treatment. A benchmarking comparison is summarized in Supplementary Table 2.

The changes in electrical resistance under tensile strain were compared between the conventional silver paste wirings, which are widely employed in stretchable devices, and the 5 wt.% LM paste wirings fabricated on Ecoflex 00-50 substrates (Fig. 3i). In the case of LM paste wirings, the resistance increased to 1.7 times the initial value under 50% tensile strain, exhibiting a nearly linear dependence on the strain. In contrast, the silver paste wiring showed a gradual increase in resistance up to 10% strain, followed by a sharp increase, with a pronounced change observed around 30% tensile strain. Under 50% stretching, the resistance of the LM wiring increased by approximately 1.6 Ω (from ~4.6 Ω to ~6.2 Ω). For a temperature sensor with a 4.5 kΩ resistance sensing element, this variation corresponds to only 0.036% of the total sensor resistance and is therefore negligible with respect to measurement accuracy. For the OTFT, the on-resistance is estimated to be in the order of 6 MΩ under $V_{DS} = -6$ V operation, rendering the 1.6 Ω wiring resistance change negligibly small in comparison. These results confirm that the resistance change of the LM wiring under stretching has no meaningful impact on either the temperature sensing performance or the OTFT characteristics.

Further, as discussed in the Introduction, electrode selection critically affects the performance of stretchable hybrid devices. Compared with the abrupt percolation-induced resistance change observed for the silver paste (Fig. 3i), the gallium-based LM paste exhibits good metallic conductivity, near-linear and reversible resistance response under strain, and stable behavior under repeated deformation, with resistance varying within 6.4–9.2 Ω over 10,000 stretch–release cycles (Supplementary Figure 6). These characteristics, together with the fine-line printability enabled by the Ni-tuned rheology, establish the 5 wt.% LM paste as a suitable interconnect for the present SRSE platform.

Finally, the practical performance of the proposed SRSE substrate, comprising the hard–soft substrate and LM wiring mixed with Ni particles, was evaluatedSupplementary Figure 7. shows the change in the normalized resistance (R/R_0) when the applied strain was increased in 50% increments. The initial resistance at 0% strain was 2.67 Ω. As the applied strain increased, the resistance increased monotonically, and a stable resistance variation along with continuous electrical conduction were confirmed over the entire strain range of 50–300%. Note that the resistance change ratio appears slightly low because the LM wiring located at the fixed ends does not undergo stretching; however, this does not affect the electrical conduction performance of the device.

Supplementary Figure 8 shows the results of cyclic tensile tests performed under each strain condition (50–300%). In this evaluation, considering the permanent (residual) strain that inevitably occurs in elastomer-based substrates, the primary criterion was to determine whether the electrical conduction was maintained when each nominal strain was repeatedly applied with respect to the initial dimension L_0. The resistance value at 0% strain after 100 break-in cycles (R_0) was used for normalization, providing a stable baseline reflecting realistic operating conditions; importantly, the following observations hold regardless of the absolute value of R_0. Under all conditions in which 50–300% cyclic stretching was applied with respect to L_0, no electrical disconnection, leakage of the LM, or fracture of the substrate occurred, and stable electrical conduction was maintained. The upper limit of R/R_0 increased monotonically with strain (approximately 1.09 at 50%, 1.20 at 100%, 1.33 at 150%, 1.39 at 200%, 1.42 at 250%, and 1.60 at 300%), whereas the lower limit converged stably to around 1.0 under all conditions, confirming the high reversibility of the device under repeated deformation.

Visual inspection results under each strain condition are presented in Supplementary Figure 9. Throughout the entire strain range of 50–300%, no wiring disconnection, LM leakage, or substrate fracture was observed, confirming that the visual integrity of the device was preserved.

Taken together, the four lines of evidence—DIC analysis, electrical characterization, cyclic testing, and visual inspection—comprehensively demonstrate that the proposed SRSE substrate withstands cyclic deformation up to 300% tensile strain with respect to its initial dimensions while stably maintaining electrical conduction.

Evaluation of temperature-sensing system

In this study, stretchable temperature-sensing systems were fabricated by mounting several types of rigid ICs on the fabricated SRSE substrate and wiring them with LM paste. Fig. 4a and b show the appearance of the temperature-sensor system before and after stretching at 50% strain, respectively. Fig. 4c shows the fabricated device attached to a human knee. Stable attachment of the fabricated device was achieved even on the knee, where bending–stretching motion frequently occurs. The temperature data acquired by the circuit elements were also successfully transmitted wirelessly and displayed in real time on external electronic devices, such as smartphones. A circuit diagram of the temperature-sensing device is shown in Supplementary Fig. 10. The microcontroller unit collects the resistance data by monitoring the changes in the thermistor according to the temperature and transmits the data to the smartphone using a Bluetooth low energy (BLE) module.

The fabricated device was stretched from 0% to 50%, and the results of the temperature measurements are shown in Fig. 4d. This graph demonstrates that stable temperature measurements were possible during stretching. The fabricated SRSE substrate, combined with the LM paste wiring, enables the entire device to accommodate mechanical deformations, thereby protecting the circuit components and maintaining stable electrical connections under stretching. LM is a promising wiring material that exhibits minimal resistance change even under large deformation, and in general wiring applications, the need for a meandering geometry is therefore less critical compared with conventional inorganic metal meander wiring. However, in temperature-sensing applications employing a thermistor, as in

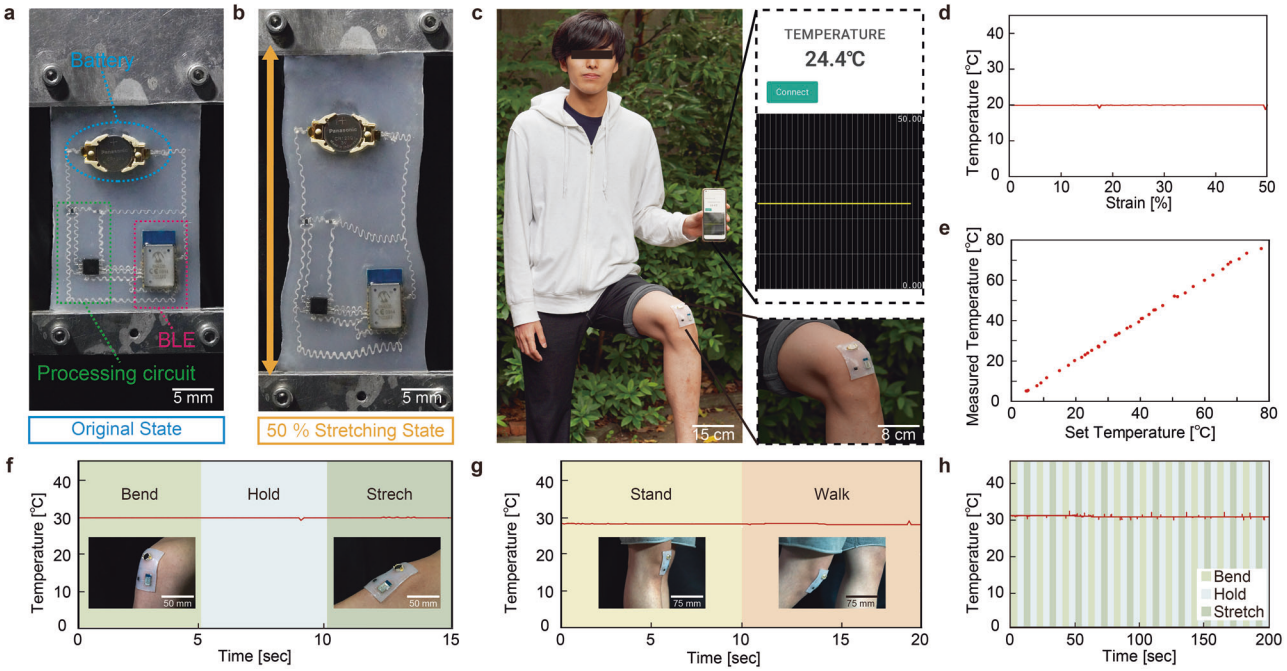


Fig. 4 | Temperature-sensing device fabricated using the proposed SRSE substrate. a Appearance of the temperature sensor before stretching. **b** Device subjected to 50% strain. The wiring was deformed owing to the stretching. In contrast, no deformation was observed in solid electronic components such as the IC. **c** Device attached to the human knee. A dedicated mobile application was developed for monitoring the temperature on the device. **d** Temperature measurements when the device was stretched to 0–50%. **e** Correlation between the actual temperature when using the device within the range of 0–80 °C and the temperature measured by the device. **f** Temperature measurement by the device worn on the knee during bending–stretching motions of the knee. Temperature measurements remain stable even under a significant deformation of the device. **g** Temperature measurement by the device during walking exercises. Temperature remains stable even under significant deformations of the device during walking. **h** Temperature measurement by the device during repeated bending and stretching tests. Temperature remains stable during repeated bending, holding, and stretching cycles.

the present study, it is desirable to minimize any resistance change in the wiring associated with device deformation. A comparison between straight and meandering LM wiring demonstrated that the meandering geometry suppressed resistance variation by up to approximately 20% at 100% strain, which represents a sufficient stretchability for wearable devices (Supplementary Fig. 11). These results suggest that meandering wiring is recommended for dynamic use environments involving high-precision sensing, such as temperature measurement.

Figure 4e shows a comparison between the measured temperature and the set temperature when the fabricated device was placed inside a constant-temperature bath. The fabricated device was designed to be worn on the human body and is capable of monitoring skin surface temperature in wearable applications. To characterize the full operational range of the device, it was evaluated over a broad temperature range of 0–80 °C. Within the constant-temperature bath, the fabricated device demonstrated accurate temperature measurements over the range of 0–80 °C, with a correlation coefficient of $R = 0.99$. A previous study presented examples of flexible temperature-sensing devices that are not stretchable but can measure temperatures from 30–110 °C[61]. However, the fabricated device uses multiple types of polymer materials as stretchable materials; therefore, its performance may vary at temperatures higher than 80 °C owing to thermal deformation. In the future, the incorporation of circuit systems that account for thermal deformations is expected to enable the realization of temperature-sensing devices across a broader temperature range, including higher temperatures.

To validate the measurement accuracy for wearable body temperature monitoring, two evaluation protocols were conducted. First, the fabricated device and a platinum resistance thermometer, serving as a reference sensor, were simultaneously placed inside a constant-temperature bath. The temperature was varied from 34 °C to 38 °C at 0.1 °C increments, and the outputs of both sensors were simultaneously recorded at each set temperature. Second, to evaluate the device response under a continuously varying temperature condition, the device and the reference thermometer were placed together and allowed to cool naturally from 38 °C to 34 °C, and the outputs of both sensors were simultaneously recorded during the cooling process. As shown in Supplementary Fig. 12, the measured values showed excellent agreement with the reference values in both protocols, with an R^2 value of 0.999 and a maximum deviation of 0.094 °C, confirming the practical accuracy of the fabricated device for wearable body temperature monitoring applications.

To further validate the device's responsiveness to actual skin temperature changes, a demonstration experiment was conducted. The corresponding video is added as Supplementary Video 1, and a comparison between the reference data and the measured temperature is presented in Supplementary Fig. 13. In this experiment, an electric heating arm warmer and a cold pack were applied to the skin, and the real-time response of the device to the resulting temperature changes was evaluated. For reference, simultaneous temperature measurements were performed using a thermocouple. Because the thermocouple was placed in direct, bare contact with the heat source, its measurement environment differed from that of the present device, resulting in a difference in the baseline temperature values. Nevertheless, with respect to the trends of temperature increase and decrease induced by heating with the arm warmer and cooling with the cold pack, the output of the present device showed excellent agreement with the response of the thermocouple. These results demonstrate that the present device can respond in real time to thermal stimuli applied to the skin, confirming its practical applicability as a wearable skin-temperature monitoring device.

To further evaluate the device performance under actual body movement conditions, temperature measurements were performed during knee bending–stretching motions. The temperature measurements obtained during knee bending–stretching motions with the fabricated device attached

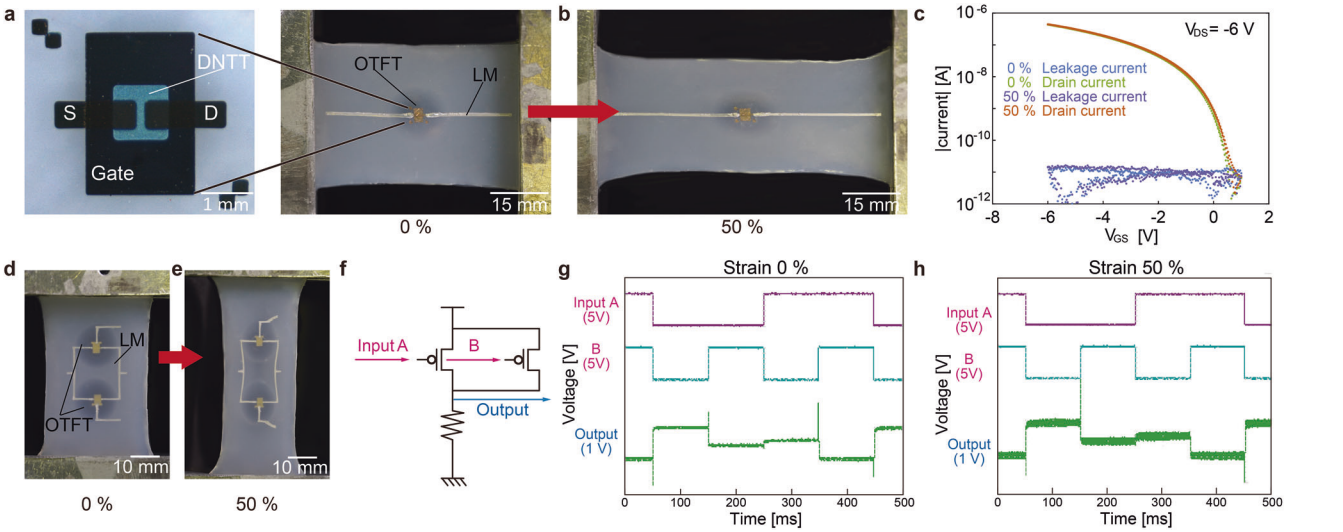


Fig. 5 | Evaluation of OTFTs fabricated on the proposed SRSE substrate. a OTFT fabricated on the SRSE substrate. **b** Stretching of the substrate with the OTFT by 50%. **c** Transmission characteristics of OTFT before and after tensile stress. The transfer characteristics were evaluated by sweeping V_{GS} from 1 V to −6 V while keeping V_{DS} fixed at −6 V. **d** NAND circuit using the OTFTs. **e** NAND circuit stretched by 50%. **f** Circuit diagram of the NAND circuit. **g** Input and output waveforms of the NAND circuit before stretching. **h** Input and output waveforms of the NAND circuit at 50% stretching.

to the knee are shown in Fig. 4f. The measured temperature remains nearly constant when the knee is flexed during the bending–stretching motion. Although slight temperature fluctuations were observed during the transition to knee extension, the measurements remained generally stable throughout the bending and stretching cycles. Fig. 4g shows the measurement results obtained during walking exercises. The maximum fluctuation range of the measured temperature remained at approximately ±2.5%, enabling stable measurements while walking. When measuring the knee temperature, no signs of significant system instability or large fluctuations in the measured temperature owing to movements were observed (Supplementary Video 2).

The results of the repeated bending–stretching tests (shown in Fig. 4h) indicate that stable temperature measurements are maintained throughout the exercise despite the repeated bending, holding, and stretching actions every 5 s, with fluctuations of only approximately ±2.5%. A previous study reported a stretchable temperature sensor worn on the wrist for real-time body-temperature measurements; the temperature fluctuations during wrist movements were reported to be within ±10%[62]. Thus, the stretchable temperature sensor in this study demonstrated superior temperature measurement accuracy.

Performance Evaluation of OTFTs Fabricated on the SRSE Substrate

In this study, OTFTs were directly fabricated on the SRSE substrates using the standard vapor-deposition process. Fig. 5a shows an OTFT fabricated on the SRSE substrate and wired using the LM paste. Fig. 5b shows the state of the same sample under 50% strain. The OTFT transfer characteristics before and after stretching are shown in Fig. 5c. The characteristics were evaluated by keeping the drain-source voltage fixed at −6 V and sweeping the gate-source voltage from 1 V to −6 V. The results showed that the OTFT fabricated in this research had an on/off ratio of 10^5 and mobility of 0.34 cm^2/Vs. No significant difference was observed between the characteristics before and after 50% stretching, suggesting that the fabricated SRSE substrate sufficiently protected the OTFT (Fig. 5c). To evaluate electromechanical stability under larger deformation, OTFTs with a thicker gate insulator layer were fabricated to ensure sufficient durability at high strain, and their transfer characteristics were measured under tensile strains of 0%, 50%, 100%, 150%, 200%, 250%, and 300% (Supplementary Fig. 14, Supplementary Table 3). The mobility averaged across all strain conditions was 0.65 cm^2/Vs, and the on/off ratio was maintained on the order of 10^5, confirming stable switching characteristics even under large deformations of up to 300%.

In addition, two OTFTs were directly fabricated on the SRSE substrate to construct NAND, AND, and NOT logic circuits. Fig. 5d, e show the appearance of the NAND circuit before and after stretching, respectively. Fig. 5f shows a schematic of the NAND circuit comprising two OTFTs connected in parallel, with the drain output read out. The results of measuring the output voltage versus the input voltages A and B before and after stretching are shown in Fig. 5g and Fig. 5h, respectively. The characteristics of the AND and NOT logic gates fabricated using the same method are shown in Supplementary Fig. 15. The fabricated AND circuit produced a high output when both the inputs were high, whereas the NOT circuit produced an inverted output based on the input. These results indicate that both the AND and NOT circuits fabricated using this process exhibit the expected logical characteristics. Thus, the fabricated OTFTs exhibit stable operation as logic circuits, and the NAND circuit continues to function normally, even after 50% stretching (Fig. 5h).

The fabricated OTFT maintained the on/off ratio of 10^5 and mobility of 0.34 cm^2/Vs at a drive voltage of 6 V, even under the maximum strain of 50%. According to the latest reviews, the mobility of OTFTs ranges from 10^{-5} to 17 cm^2/Vs, and on/off ratios of 10^2–10^{10} have been achieved[63]. The highest-level OTFTs use 2,7-dioctyl[1]benzothieno[3,2-b][1]benzothiophene (C8-BTBT) as the semiconductor layer, achieving the maximum and average mobilities of 43 cm^2/Vs and 25 cm^2/Vs, respectively, at the drive voltages of −15 to −40 V[64]. In addition, the amorphous indium-gallium-zinc-oxide (*a*-IGZO)-based stretchable TFT matrix array on SU-8 has been reported to achieve an on/off ratio of approximately 1×10^8 and mobility of 12.7 cm^2/Vs at a drive voltage of 5 V[65]. Although the fabricated OTFTs exhibited a lower mobility than those reported in a previous study, they were sufficiently practical from the perspective of the drive voltage. The lower mobility may have been caused by the surface roughness of the epoxy layer and the tightness of the mask seal used in the fabrication process of the OTFTs. These issues are expected to be improved by optimizing the hard layer and setting up a mask material in the future.

Nevertheless, the SRSE substrate proposed in this study allows for greater versatility in material selection for TFTs and OTFTs because the OTFTs can be fabricated directly using standard vapor-deposition methods. Furthermore, its application can possibly be extended to other thin-film electronic devices such as LEDs, thin-film sensors, and photodiodes.

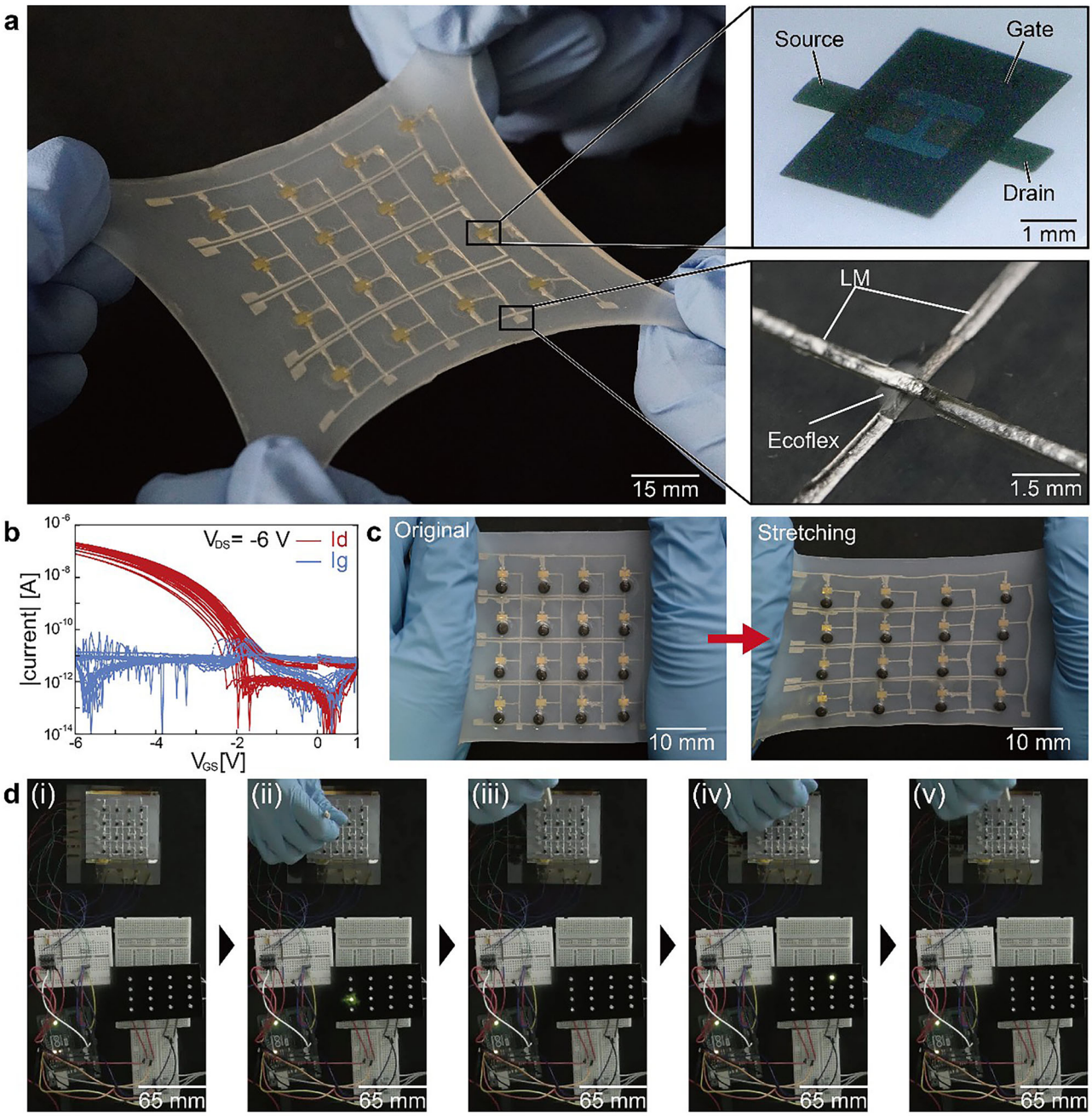


Fig. 6 | Stretchable active matrix using OTFTs directly fabricated on the SRSE substrate. a Stretchable active matrix. The OTFT was fabricated on the rigid layer. The active-matrix circuit was formed by LM paste wiring. The 3D wiring structure was formed by insulating the intersection points of the LM paste using Ecoflex. **b** Transmission characteristics of a 15-pixel OTFT on this active matrix. The transfer characteristics were evaluated by sweeping V_{GS} from 1 V to −6 V while keeping V_{DS} fixed at −6 V. **c** The pressure-sensing composite was mounted on this active matrix, stretching the matrix circuit by 50%. **d** When pressure was applied to the active matrix with the pressure-sensing composite, pressure was detected at each pixel.

16-pixel OTFTs were fabricated on the SRSE substrate and interconnected using LM paste and 3D LM wiring through Ecoflex to realize an active matrix (Fig. 6a). The active matrix can be bent and stretched (Supplementary Fig. 16). Fig. 6b summarizes the transfer characteristics of the 15 pixels that were successfully driven out of the 16 fabricated OTFT pixels. The defective pixel exhibited dominant gate leakage current, attributed to mechanical damage from the metal-mask edge and particle contamination on the epoxy resin surface. Future yield improvements are expected through mask-surface coating and enhanced cleanroom processing.

Supplementary Fig. 17 shows the drain current values at different cycle numbers when the substrate is repeatedly stretched to 50% strain. This demonstrates that the OTFTs maintained their performance even after 100 stretching cycles, confirming that the 16-pixel SRSE substrate can be stretched and compressed while protecting the device section.

Furthermore, a pressure-sensing matrix circuit was fabricated by mounting pressure sensors on each drain-electrode side of the stretchable active matrix. The images before and after stretching are shown in Fig. 6c. A circuit diagram of the matrix is shown in Supplementary Fig. 18. This active-matrix circuit, which can detect pressure, was driven to illuminate the LED at a location depending on the desired pressure load (Fig. 6dSupplementary Video 3,). This pressure-sensing stretchable active matrix uses OTFTs as the active elements and pressure sensors as the driving elements. This research

Table 1 | Stretchable active-matrix comparison chart

Ref	Author	TFT Type	Stretchability Approach	Stretchability	Material Dependence	Integration Density	Mobility (cm^2 / V· s)	Fabrication Process	Year
48	Wang et al.	organic	Material approach polymer blend	100	—	100	0.82	Indirect	2018
66	Oh et al.	organic	Material approach polymer composite	100	—	25	0.076	Indirect	2019
67	Liu et al.	organic	Material and Structural approach rigid islands + soft matrix & polymer composite	100	—	25	0.56	Indirect	2020
68	Xu et al.	organic	Material approach intermolecular crosslinking	100	—	20	1.5	Direct	2019
69	Sim et al.	organic	Material approach Nano-/mesoscale structure introduction	50	—	64	3.57	Indirect	2019
35	Matsuhisa et al.	organic	Structural approach rigid islands + soft matrix	110	○	144	1.8	Indirect	2015
75	Wang et al.	organic	Structural approach rigid islands + soft matrix	100	○	100	0.62	Indirect	2021
65	Kang et al.	Inorganic	Structural approach rigid islands + soft matrix	50	○	49	12.7	Indirect	2024
–	This research	organic	Structural approach rigid islands + soft matrix	300	○	16	0.65	Direct	2026

achieved a total 16-pixel matrix of 4 × 4 pixels, with a pressure sensor mounted as the drive element on the drain electrode of each OTFT.

The operating principles are as follows. The OTFT was selected to detect the pressure from the pressure sensor by sequentially applying a voltage to the gate electrode. To ensure impedance matching between the OTFT and pressure sensor, the latter was required to exhibit a resistance below 10^6 Ω under the applied pressure and 10^8 Ω when unloaded (Supplementary Fig. 19). In this study, a pressure sensor was fabricated by mixing a polymer material with nickel powder. When pressure was applied, the resistance of the sensor decreased, enabling pressure detection at specific locations via OTFT scanning. When pressure was detected, the corresponding LED was illuminated.

The fabricated stretchable OTFT active-matrix substrate was compared with previously fabricated stretchable TFT and OTFT active-matrix substrates (Table 1). Previous studies on stretchable TFTs and OTFTs can be broadly categorized into material-based (intrinsically stretchable semiconductor-based) and structural approaches. The material-based approach aims to impart stretchability to inherently non-stretchable semiconductor materials. Methods such as blending semiconductors with polymers[48,66,67], creating composites[67], utilizing molecular-level interactions for stretchability[68], and introducing nanoscale and mesoscale structures[69] have been reported. Ideally, the material-based approach should enable enhanced functionality and integration. However, it faces challenges such as reduced mobility[70], phase separation[71], reproducibility issues[72], and increased complexity in material design[73].

In contrast, the structural approach[35,65,74] achieves both high stretchability and mechanical stability by spatially separating the stretchable and non-stretchable regions. Generally, TFT devices are located on rigid (non-stretchable) islands, which are interconnected by stretchable conductive wiring. Because this method requires buffer spaces between the rigid and stretchable components, it is less advantageous for high-density integration than the material-based approach. However, it offers significant advantages such as high carrier mobility, excellent cyclic strain endurance, and a wide selection of device materials, as the established knowledge from solid-state electronics can be directly applied to stretchable devices. Therefore, in the current development of stretchable integrated circuits, it is necessary to appropriately select or combine these two approaches depending on the specific application.

Previous research on stretchable TFT or OTFT active matrices using a structural approach employed indirect methods, such as transfer methods[65,74] or embedding methods[35], for TFT or OTFT implementation. The fabrication of TFT or OTFT active matrices using indirect methods leads to increased complexity in device fabrication, ultimately leading to a bottleneck when scaling up to multipixel integration or adding other functions.

The SRSE substrate developed in this study, which enables direct fabrication using vapor deposition, contributes to the improved processability of stretchable TFT and OTFT substrates when compared with that in conventional indirect mounting methods. This achieves greater freedom in material selection and reduces the risk of TFT and OTFT damage. Furthermore, the adoption of a hybrid soft–rigid structure enables the additional integration of sensors, such as pressure sensors, and general-purpose rigid IC components on top of the TFT and OTFT matrices, thereby achieving both flexibility and extensibility of the device.

Although the fabricated SRSE substrate did not achieve the maximum pixel density of the stretchable active matrix when using other structural approaches, it indicated the potential for implementing multipixel thin-film electronic devices on the same substrate through material selection and optimization of the processing conditions. Therefore, this technology is expected to be applied as a multifunctional, highly integrated, and stretchable electronic substrate in the future.

Discussion

In this study, we developed an SRSE substrate designed for the direct fabrication and integration of OTFTs and rigid IC components,

respectively. The fabricated SRSE substrate featured a composite structure incorporating three materials with distinct Young's moduli—Ecoflex 00-50, PDMS, and epoxy resin—enabling it to withstand strains of up to 300%. The planar surface of the epoxy resin, acting as a rigid layer, facilitated both the direct mounting of IC chips and high-fidelity fabrication of OTFTs. To validate the operational stability of the system, we integrated a temperature sensor with a BLE module and developed a mobile application for real-time monitoring. The sensor maintained stable data acquisition and wireless transmission, even under 50% strain and during active walking motions. Furthermore, the OTFTs, fabricated using the standard deposition technique, exhibited an on/off ratio of 10^5 and a mobility of 0.34 cm^2/Vs. Using these OTFTs, a 16-pixel active matrix was successfully integrated with a pressure sensor, demonstrating effective spatial pressure detection. These results confirm that the fabricated SRSE substrate is a highly effective platform for the direct fabrication and integration of stretchable electronic systems.

Modulus-gradient strategies in SRSE substrates can be broadly classified into three categories (Supplementary Table 4): (i) Spatial/Density Control[21,75,76], in which photolithography-based spatial modulation of the crosslink density yields stiffness ratios on the order of 10^4 but suffers from long-term stability concerns; (ii) Geometrical/Structural Gradient[19,23,24,77], in which anchor structures or biomimetic geometries surrounding the rigid layer realize stiffness ratios exceeding 10^4 at the cost of enlarged interlayer dimensions that hinder miniaturization and high-density integration; and (iii) Material-based modulus engineering[65,78], in which multiple materials with different Young's moduli are physically combined to form a gradient, providing direct access to functional material properties—as exemplified by a recent material-based design that integrated rigid chips and flexible sensors with a stiffness ratio in the order of 10^3 between the two components[78]—but typically limited to stiffness ratios of 10^2–10^3 owing to interfacial adhesion challenges between dissimilar materials. The proposed SRSE substrate belongs to category (iii). However, by introducing an intermediate-modulus PDMS layer between the epoxy rigid layer and the Ecoflex soft layer, the substrate achieves a stiffness ratio in the order of 10^4—comparable to geometric gradient approaches—while preserving the material versatility characteristic of material-based design. This combination, together with the planar and process-compatible surface of the rigid layer, simultaneously enables the direct fabrication of OTFTs and the integration of rigid IC components on a single stretchable platform, providing a clear differentiation from conventional hybrid integration strategies.

Compared with our previous report, which focused on reinforcing the junctions between LM interconnects and rigid circuits fabricated on planar polyimide substrates, the present study introduces three key advances. First, a local patterning technique for the epoxy layer enables the construction of arbitrarily shaped "rigid islands" embedded within the flexible substrate, providing high geometric design flexibility for mounting a wide variety of rigid components rather than only reinforcing pre-defined interconnect junctions. Second, the high surface planarity and thermal stability of the patterned epoxy rigid regions allow standard vacuum-deposition processing to be performed directly on the substrate, enabling on-substrate fabrication of high-quality OTFTs in addition to the conventional integration of prefabricated components. Third, by considering interlayer affinity from the material-selection stage and chemically bonding the rigid–intermediate interface through excimer treatment, an adhesive-free robust interfacial structure is realized; combined with a dome-shaped multilayer architecture, the substrate withstands a tensile strain of 300% and endures 1500 cycles under 100% strain, substantially exceeding the durability of the silicone-rubber-adhesive-based design used previously. While the previous report focused on the localized issue of junction durability, the present work redesigns the entire rigid–soft composite substrate, enabling both direct fabrication and stable integration of diverse devices.

This study provides a versatile platform for bridging the gap between intrinsically stretchable interconnects and high-performance rigid devices. Our findings provide a valuable reference for implementing stable wearable electronics for living organisms or objects undergoing large deformations. Future work could expand this platform by integrating sensing arrays with machine-learning algorithms. Such a system would enable sophisticated data analysis by actively controlling the multimodal sensors mounted on SRSE substrates. However, some challenges remain: increasing the density of rigid components may limit the overall deformability; and the fundamental interfacial adhesion between the soft, intermediate, and rigid layers requires further optimization. By overcoming the tradeoff between mechanical flexibility and electronic performance using this approach, we can move closer to the realization of practical applications of stretchable substrates. Addressing the existing issues through material refinement and fully flexible integration will pave the way for mass-produced stretchable substrates and accelerate the widespread implementation of stretchable electronics.

Methods

Manufacturing of SRSE Substrates

A substrate with a convex dome-shaped pattern was fabricated using a high-resolution 3D printer (AGILISTA-3200, Keyence). Polyvinyl alcohol (PVA; 10 g, Kanto Chemical) was mixed with 100 mL deionized water. The mixture was stirred while heating to 120 °C to dissolve the PVA, producing an aqueous solution of PVA. Using a spin coater (MS-B100, MIKASA), the PVA aqueous solution was coated onto a polyethylene naphthalate (PEN) film (125 μm) attached to an acrylic plate at a rotation speed of 500 rpm and coating time of 30 s. This was followed by curing in a 70 °C oven for 30 min. After drying, the PEN film was peeled off from the acrylic plate.

The PDMS base (KE-1606, Shin-Etsu Silicones) and curing agent (CAT-RG, Shin-Etsu Silicones) were mixed in a mass ratio of 10:1. Using a planetary mixer (ARE-310, THINKY), the mixture was stirred at 2000 rpm for 2 min and degassed at 2200 rpm for 1 min. After applying a release agent (Ease Release, Smooth-On) to the patterned substrate, PDMS was applied to cover an area larger than that of the patterned shape. It was then cured in a 70 °C oven for 1 hour. Ecoflex 00-50 for the base (Part A, Smooth-On) and the hardener (Part B, Smooth-On) were mixed in a 1:1 mass ratio. The mixture was degassed for 5 min in a vacuum desiccator (VLBR, ASONE) and coated using a spin coater at 300 rpm for 30 s. After application, it was cured in a 70 °C oven for 10 min. The spin coating and curing of Ecoflex 00-50 were repeated. The PVA-film side of the SRSE support substrate was adhered to the uncured Ecoflex 00-50 and cured in a 70 °C oven for 10 min. Subsequently, the Ecoflex 00-50, PDMS, and support substrate were peeled off from the patterned substrate, and the PEN film side was adhered to a glass plate.

Then, a PI film (3 M, thickness 125 μm) was cut to the same dimensions as those of the patterned substrate using a laser cutter (MD-T1000W, Keyence), and subjected to excimer processing for 90 s using an excimer lamp light source (FLAT EXCIMER EX-mini, Hamamatsu Photonics). The epoxy resin base (jER828, Mitsubishi Chemical) and hardener (1,3-BAC, Mitsubishi Gas Chemical) were mixed at a mass ratio of 100:19.1. Using a planetary centrifugal mixer, the mixture was stirred at 2000 rpm for 4 min and degassed at 2200 rpm for 2 min. It was then cast onto the PI film and screen-printed using the side of a glass pipette. The PI film was peeled off, and the substrate was placed on a hot plate, heated from room temperature to 120 °C, and held at that temperature for 30 min to cure.

Fabrication of temperature-sensing devices

Solid electronic components were fixed to the SRSE substrate using an adhesive. After LM paste wiring, each component was covered with a protective layer tailored to the size of the substrate layers in the following order: epoxy resin, PDMS, and Ecoflex 00-50.

Fabrication of OTFTs

The OTFTs were fabricated using a vacuum evaporator (EX200, ULVAC), plasma cleaner (PC-300, SAMCO), parylene coater (PDS 2010 LABCOTER, SCS), and laser cutter (MD-T1000, Keyence). A polyimide film, with patterning that exposes only the epoxy portion, was attached to the SRSE

substrate for protection of the substrate. A metal mask was positioned over the gate electrode. Al was flash deposited at 100 nm using a vacuum deposition machine to form the gate electrode. The insulating layer was fabricated by subjecting the aluminum electrode to oxygen plasma treatment at 100 W for 3 min using a plasma cleaner, followed by the deposition of parylene diX-SR (Daisan Kasei Co., Ltd.) at a thickness of 100 nm using a parylene coater. Subsequently, a DNTT metal mask was set and DNTT (Nippon Kayaku Co., Ltd.), which served as the organic semiconductor layer, was deposited at a thickness of 30 nm using a vacuum evaporator at a rate of 0.3 Å/s. Subsequently, the source and drain metal masks were positioned, and the source and drain electrodes were deposited to a thickness of 50 nm by evaporating Au at 3 Å/s. The channel length and width were 200 μm and 500 μm, respectively. To protect the DNTT layer, parylene diX-SR was redeposited at a thickness of 600 nm using the parylene coater. Holes were opened from the top of each electrode using a laser cutter to ensure electrical contact. The output settings of the laser cutter were as follows: laser power 5.0%, scanning speed 20 mm/s, Q-switch frequency 1 kHz, and number of print cycles 1. Finally, the OTFTs were fabricated by depositing Au at 10 nm/s using a vacuum evaporator to establish contact with each electrode through the holes.

Fabrication of LM paste and wires

GaInSn (15.2 g; Ga:In:Sn = 68.5:21.5:10) (zairyo-ya.com) and 0.8 g of Ni powder (Alfa Aesar, < 50 μm) were mixed using a rotating-revolving mixer at 2000 rpm for 20 min. Then, ultrasonic processing was performed on the LM and Ni powder using an ultrasonic homogenizer (Branson digital Sonifier SFX 550, Branson) with the following settings—output energy 6.10 kJ, ON time 2 s, OFF time 4 s, total ON time 1 min 52 s—and a 1/8 microtip. After processing, the mixture was oxidized by exposing it to air for one day to produce an LM paste. LM wiring was fabricated by attaching a laser-cut patterned PI film, subjecting it to excimer treatment, and then screen printing the LM paste.

3D wiring

The Ecoflex 00-50 base material and hardener were mixed in a 1:1 mass ratio. The mixture was degassed for 5 min in a vacuum desiccator and applied to the wiring intersection points. After curing for 10 min in a 70 °C oven, the LM paste was screen-printed using the same procedure as followed for manufacturing the wiring.

Pressure-sensitive conductive composite

Ni powder (5.0 g) and Skin Tite (1.5 g; Smooth-On) Base Material (Component A) were mixed using a centrifugal-rotary mixer at 2000 rpm for 5 min. After mixing, 1.5 g of the Skin Tite hardener (Component B) was added and mixed using the same rotary-orbital mixer at 2000 rpm for 2 min. The mixture was then transferred to an acrylic mold made from a 2 mm-thick acrylic sheet before curing. A weight was placed on top, and the mold was cured in a 70 °C oven for 10 min. After curing, a pressure sensor was fabricated by demolding using a biopsy trephine (BP-30F, KAI INDUSTRIES).

Substrate distortion analysis

Substrate distortion analysis was performed using DIC analysis with a numerical analysis software (MATLAB, MathWorks). The substrate was colored using a black body spray (TASCO) and dried at room temperature for 30 min. Subsequently, the colored substrate was deformed using a high-precision, high-accuracy automatic stage (OSMS26-50X, SIGMAKOKI) and a 3-axis stage controller (HSC-103, SIGMAKOKI). This process was recorded directly from above using a video camera. The frames were extracted from the video at one-second intervals, and the strain was measured by analyzing the changes in the pattern on the substrate using numerical analysis software.

Tensile break test of substrates

Tensile break tests were conducted on the substrates using a tensile-testing machine (EZ-LX, SHIMADZU). The substrates were standardized into rectangular shapes. The tensile-testing machine measured the applied load while pulling the substrate until it broke.

Measurement of roundness of epoxy layer

The roundness of the epoxy layers was measured using a laser microscope. The roundness was determined by altering the curvature of the convex patterns on the patterned substrate and measuring the surface height of the epoxy layer on the SRSE substrate at each curvature using a laser microscope.

Preparation of silver paste

Styrene butadiene styrene (SBS; 150 mg), polystyrene-block-polybutadiene-block-polystyrene (Sigma-Aldrich), and 1 mL of tetrahydrofuran were added and stirred for 30 min to dissolve the SBS. Then, 450 mg of silver flakes (10 μm, Sigma Aldrich) were added, and stirring was continued for an additional hour to prepare the paste.

Measurement of tensile resistance change in wiring

The tensile resistance change in the wiring was measured using a high-precision, precision-type automatic stage, 3-axis stage controller, and an LCR meter (ZM2376, NF). A PI film with arbitrarily patterned lengths and thicknesses was affixed to Ecoflex 00-50. After excimer processing, the LM and silver pastes were screen-printed onto the film. Each sample was pulled using a high-precision, high-accuracy automatic stage and 3-axis stage controller while measuring the resistance with an LCR meter.

Actual temperature measurement of temperature-sensor devices

Actual temperature measurements of the temperature-sensor devices were performed using a constant-temperature drying oven (OFW-600B, ASONE). The measured temperature obtained by the thermocouple and the temperature displayed on the device were compared for temperature settings of 5–80 °C.

Temperature measurement during tensile testing of temperature-sensor devices

Temperature measurements during tensile testing of the temperature-sensor devices were performed using a high-precision, high-accuracy automatic stage and 3-axis stage controller. The temperature was measured continuously while varying the tensile stress from 0 to 50%.

Measurement of OTFT transfer characteristics

The OTFT transfer characteristics were measured using a probe station (705 B, Micronics, Japan) and semiconductor device analyzer (B1500A, KEYSIGHT). First, the fabricated OTFT substrate was placed on a probe-station stage. To avoid damaging the OTFT electrodes, gold wires were connected to the tips of the tungsten needles, and contact was made between each OTFT electrode and the gold wire. This setup was analyzed using a semiconductor device analyzer to measure the transfer characteristics.

Pressure-sensor pressure test

A pressure test for the pressure sensor was conducted using a vertical motorized measurement stand (KV-50N, IMADA), a digital force gauge (ZTA-20N, IMADA), and an LCR meter. The left and right edges of the bottom surface of the fabricated pressure sensor were connected to the LM wiring. Pressure was applied from the top surface using a digital force gauge fixed to a vertical motorized test stand, and the resistance during this process was simultaneously measured using the LCR meter.

Experiments with human research participants

The research protocol was approved by the ethics committee of the Yokohama National University Graduate School of Engineering Science (no. 2020-16, approved on February 12, 2021). Written informed consent to publish identifiable images and details was obtained from the individual, who is also a co-author of this manuscript.

Data availability

All data generated or analyzed during this study are included in this published article and its supplementary information files. The underlying code for this study is not publicly available but may be made available to qualified researchers on reasonable request from the corresponding author.

Code availability

The underlying code for this study is not publicly available but may be made available to qualified researchers on reasonable request from the corresponding author.

Received: 5 February 2026; Accepted: 4 July 2026;
Published online: 14 July 2026

References

1. Wu, Y. et al. Piezoresistive stretchable strain sensors with human machine interface demonstrations. *Sens. Actuators A: Phys.* **279**, 46–52 (2018).
2. You, I. et al. Stretchable E-Skin Apexcardiogram sensor. *Adv. Mater.* **28**, 6359–6364 (2016).
3. Xu, H. et al. An ultra-stretchable, highly sensitive and biocompatible capacitive strain sensor from an ionic nanocomposite for on-skin monitoring. *Nanoscale* **11**, 1570–1578 (2019).
4. Wu, Z. et al. Ultrasensitive, stretchable, and fast-response temperature sensors based on hydrogel films for wearable applications. *ACS Appl. Mater. Interfaces* **13**, 21854–21864 (2021).
5. Ge, G. et al. Stretchable, transparent, and self-patterned hydrogel-based pressure sensor for human motions detection. *Adv. Funct. Mater.* **28**, 1802576 (2018).
6. Jafari, A. Stretchable electronics: advances in elastic conductive fibers for multifunctional applications. *Org. Electron.* **135**, 107145 (2024).
7. Huang, Z. et al. Three-dimensional integrated stretchable electronics. *Nat. Electron* **1**, 473–480 (2018).
8. Kim, S. H. et al. Strain-invariant stretchable radio-frequency electronics. *Nature* **629**, 1047–1054 (2024).
9. Choi, G. et al. Omnidirectionally stretchable organic transistors for use in wearable electronics: ensuring overall stretchability by applying nonstretchable wrinkled components. *ACS Appl. Mater. Interfaces* **12**, 32979–32986 (2020).
10. Kim, D. W., Kong, M. & Jeong, U. Interface design for stretchable electronic devices. *Adv. Sci.* **8**, 2004170 (2021).
11. Lee, W., Kim, Y., Lee, M. Y., Oh, J. H. & Lee, J. U. Highly stretchable fiber transistors with all-stretchable electronic components and graphene hybrid electrodes. *Org. Electron.* **69**, 320–328 (2019).
12. Lu, L. et al. Stretchable all-gel organic electrochemical transistors. *Nat. Commun.* **16**, 3831 (2025).
13. Hou, W., Liao, Q., Xie, S., Song, Y. & Qin, L. Prospects and challenges of flexible stretchable electrodes for electronics. *Coatings* **12**, 558 (2022).
14. Oh, H. et al. High density integration of stretchable inorganic thin film transistors with excellent performance and reliability. *Nat. Commun.* **13**, 4963 (2022).
15. Jiao, H. et al. Intrinsically stretchable all-carbon-nanotube transistors with styrene–ethylene–butylene–styrene as gate dielectrics integrated by photolithography-based process. *RSC Adv.* **10**, 8080–8086 (2020).
16. Xu, S. et al. Soft microfluidic assemblies of sensors, circuits, and radios for the skin. *Science* **344**, 70–74 (2014).
17. Liu, Y. et al. Epidermal mechano-acoustic sensing electronics for cardiovascular diagnostics and human-machine interfaces. *Sci. Adv.* **2**, e1601185 (2016).
18. Lin, R., Li, Y., Mao, X., Zhou, W. & Liu, R. Hybrid 3D printing all-in-one heterogenous rigidity assemblies for soft electronics. *Adv. Mater. Technol.* **4**, 1900614 (2019).
19. Gul, O. et al. Bioinspired interfacial engineering for highly stretchable electronics. *Nat. Commun.* **16**, 1337 (2025).
20. Gul, O. et al. Bioinspired omnidirectional interface engineered flexible island for highly stretchable electronics. *Small* **21**, 2410247 (2025).
21. Pan, X. et al. Strain-engineered gradient-modulus platforms for mechanically robust and conformable hybrid electronics. *Adv. Funct. Mater.* **36**, e75046 (2026).
22. Byun, J. et al. Fully printable, strain-engineered electronic wrap for customizable soft electronics. *Sci. Rep.* **7**, 45328 (2017).
23. Yang, J. C. et al. Geometrically engineered rigid island array for stretchable electronics capable of withstanding various deformation modes. *Sci. Adv.* **8**, eabn3863 (2022).
24. Lim, M. S. et al. Two-dimensionally stretchable organic light-emitting diode with elastic pillar arrays for stress relief. *Nano Lett.* **20**, 1526–1535 (2020).
25. Liu, Y. et al. Stretchable motion memory devices based on mechanical hybrid materials. *Adv. Mater.* **29**, 1701780 (2017).
26. Lee, H. Recent advances in transfer printing of inorganic thin films for flexible hybrid systems. *Micro Nano Syst. Lett.* **13**, 17 (2025).
27. Linghu, C., Zhang, S., Wang, C. & Song, J. Transfer printing techniques for flexible and stretchable inorganic electronics. *npj Flex. Electron* **2**, 26 (2018).
28. Tang, J. et al. Highly stretchable electrodes on wrinkled Polydimethylsiloxane substrates. *Sci. Rep.* **5**, 16527 (2015).
29. Silva, C. A. et al. Liquid metal based island-bridge architectures for all printed stretchable electrochemical devices. *Adv. Funct. Mater.* **30**, 2002041 (2020).
30. Kim, T.-H., Bao, C., Chen, Z. & Kim, W. S. 3D printed leech-inspired origami dry electrodes for electrophysiology sensing robots. *npj Flex. Electron* **6**, 5 (2022).
31. Zhang, C. et al. Stretchable transparent electrodes with solution-processed regular metal mesh for an electroluminescent light-emitting film. *ACS Appl. Mater. Interfaces* **10**, 21009–21017 (2018).
32. Kang, C., Kim, S.-W., Kim, W., Choi, D. & Kim, H.-K. Stretchable and flexible snake skin patterned electrodes for wearable electronics inspired by kirigami structure. *Adv. Mater. Interfaces* **10**, 2202477 (2023).
33. Bhagavatheswaran, E. S. et al. Construction of an interconnected nanostructured carbon black network: development of highly stretchable and robust elastomeric conductors. *J. Phys. Chem. C.* **119**, 21723–21731 (2015).
34. Wang, Y. et al. A highly stretchable, transparent, and conductive polymer. *Sci. Adv.* **3**, e1602076 (2017).
35. Matsuhisa, N. et al. Printable elastic conductors with a high conductivity for electronic textile applications. *Nat. Commun.* **6**, 7461 (2015).
36. Kim, M. et al. Nanowire-assisted freestanding liquid metal thin-film patterns for highly stretchable electrodes on 3D surfaces. *npj Flex. Electron* **6**, 99 (2022).
37. Pyo, S. et al. Carbon nanotube-graphene hybrids for soft electronics, sensors, and actuators. *Micro Nano Syst. Lett.* **10**, 9 (2022).
38. Wójkowska, K. et al. Highly conductive silver layers with self-healing abilities for stretchable electronics and beyond. *Adv. Compos. Hybrid. Mater.* **9**, 216 (2026).
39. Ma, J. et al. Microconfined assembly of high-resolution and mechanically robust EGaIn liquid metal stretchable electrodes for wearable electronic systems. *Adv. Sci.* **11**, 2402818 (2024).
40. Naserifar, N., LeDuc, P. R. & Fedder, G. K. Material gradients in stretchable substrates toward integrated electronic functionality. *Adv. Mater.* **28**, 3584–3591 (2016).
41. Moser, R. et al. From playroom to lab: tough stretchable electronics analyzed with a tabletop tensile tester made from toy-bricks. *Adv. Sci.* **3**, 1500396 (2016).
42. Yao, B. et al. Ultrasensitive, highly stable, and stretchable strain sensor using gated liquid metal channel. *Adv. Funct. Mater.* **34**, 2314298 (2024).

43. Waddell, E. A. et al. Surface modification of Sylgard 184 polydimethylsiloxane by 254 nm excimer radiation and characterization by contact angle goniometry, infrared spectroscopy, atomic force and scanning electron microscopy. *Appl. Surf. Sci.* **254**, 5314–5318 (2008).
44. Owen, M. J. & Smith, P. J. Plasma treatment of polydimethylsiloxane. *J. Adhes. Sci. Technol.* **8**, 1063–1075 (1994).
45. Khoun, L. & Hubert, P. Cure shrinkage characterization of an epoxy resin system by two in situ measurement methods. *Polym. Compos.* **31**, 1603–1610 (2010).
46. Jørgensen, J. K., Maes, V. K., Mikkelsen, L. P. & Andersen, T. L. A precise prediction of the chemical and thermal shrinkage during curing of an epoxy resin. *Polymers* **16**, 2435 (2024).
47. Kang, S. J. et al. Geometric effect of channel on device performance in pentacene thin-film transistor. *Jpn. J. Appl. Phys.* **43**, 7718 (2004).
48. Wang, S. et al. Skin electronics from scalable fabrication of an intrinsically stretchable transistor array. *Nature* **555**, 83–88 (2018).
49. Liao, Z. et al. On the stress recovery behaviour of Ecoflex silicone rubbers. *Int. J. Mech. Sci.* **206**, 106624 (2021).
50. Zhu, S. et al. Interfacial tension of Ga, E-GaIn, Galinstan, and GaInSnBiZn high-entropy alloy. *J. Mater. Eng. Perform.* **33**, 2369–2378 (2024).
51. Guo, R. et al. Ni-GaIn amalgams enabled rapid and customizable fabrication of wearable and wireless healthcare electronics. *Adv. Eng. Mater.* **20**, 1800054 (2018).
52. Daalkhaijav, U., Yirmibesoglu, O.D., Walker, S. & Mengüç, Y. Rheological modification of liquid metal for additive manufacturing of stretchable electronics. *Adv. Mater. Technol.* **3**, 1700351 (2018).
53. Kaneko, T. et al. Printed bilayer liquid metal soft sensors for strain and tactile perception in soft robotics. *Adv. Mater. Technol.* **8**, 2300436 (2023).
54. Gul, O., Ahn, J., Kim, H. J., Yu, X. & Park, I. Mechanochemically activatable liquid metal powders for sustainable, reconfigurable and versatile electronics. *Adv. Funct. Mater.* **36**, e27396 (2026).
55. Park, Y.-G. et al. High-resolution, reconfigurable printing of liquid metals with three-dimensional structures. *Sci. Adv.* **5**, eaaw2844 (2019).
56. Li, X. et al. Non-loss engraved circuit patterning method of semi-liquid metal for precision recyclable multi-substrate circuits. *Nat. Commun.* **16**, 11690 (2025).
57. Zhang, J. et al. Controlling the oxidation and wettability of liquid metal via femtosecond laser for high-resolution flexible electronics. *Front. Chem.* **10**, 965891 (2022).
58. Lee, D. H. et al. Universal cryogenic transfer of liquid metal particles in polymers for wafer-scale stretchable integrated electronics. *Nat. Commun.* **17**, 3248 (2026).
59. Park, C. W. et al. Photolithography-based patterning of liquid metal interconnects for monolithically integrated stretchable circuits. *ACS Appl. Mater. Interfaces* **8**, 15459–15465 (2016).
60. Shang, J. et al. Fully screen printed stretchable liquid metal multilayer circuits using green solvents and scalable water-spray sintering. *npj Flex. Electron* **9**, 19 (2025).
61. Shih, W.-P. et al. Flexible temperature sensor array based on a graphite-polydimethylsiloxane composite. *Sensors* **10**, 3597–3610 (2010).
62. Kang, S. et al. Laser-processed stretchable-gradient interconnection-based temperature sensor for a real-time monitoring system. *ACS Appl. Electron. Mater.* **3**, 5601–5607 (2021).
63. Ajayan, J. et al. An intensive study on organic thin film transistors (OTFTs) for future flexible/wearable electronics applications. *Micro Nanostruct.* **187**, 207766 (2024).
64. Yuan, Y. et al. Ultra-high mobility transparent organic thin film transistors grown by an off-centre spin-coating method. *Nat. Commun.* **5**, 3005 (2014).
65. Kang, S.-H. et al. Full integration of highly stretchable inorganic transistors and circuits within molecular-tailored elastic substrates on a large scale. *Nat. Commun.* **15**, 2814 (2024).
66. Oh, J. Y. et al. Stretchable self-healable semiconducting polymer film for active-matrix strain-sensing array. *Sci. Adv.* **5**, eaav3097 (2019).
67. Liu, J. et al. Fully stretchable active-matrix organic light-emitting electrochemical cell array. *Nat. Commun.* **11**, 3362 (2020).
68. Xu, J. et al. Multi-scale ordering in highly stretchable polymer semiconducting films. *Nat. Mater.* **18**, 594–601 (2019).
69. Sim, K. et al. Fully rubbery integrated electronics from high effective mobility intrinsically stretchable semiconductors. *Sci. Adv.* **5**, eaav5749 (2019).
70. Wu, H.-C. et al. Highly stretchable polymer semiconductor thin films with multi-modal energy dissipation and high relative stretchability. *Nat. Commun.* **14**, 8382 (2023).
71. Zhou, Q. et al. Biomimetic fibrous semiconducting micromesh via tuning phase separation for high-performance stretchable optoelectronic synapses. *Nat. Commun.* **16**, 8483 (2025).
72. Wang, Z., Liu, Y. & Zhao, Y. Advances in stretchable polymer semiconductors: design strategies and applications inhuman-machine interaction and bioelectronics. *Advanced Mater*. e07519. https://doi.org/10.1002/adma.202507519 (2025).
73. Mun, J. et al. A design strategy for high mobility stretchable polymer semiconductors. *Nat. Commun.* **12**, 3572 (2021).
74. Wang, W. et al. Strain-insensitive intrinsically stretchable transistors and circuits. *Nat. Electron* **4**, 143–150 (2021).
75. Zhao, W. et al. Modulus engineered substrate with vertical soft interconnects for ultra-stable stretchable multilayer electronic systems. *Adv. Mater.* **38**, e72292 (2026).
76. Sun, B. et al. Gradient modulus strategy for alleviating stretchable electronic strain concentration. *Adv. Funct. Mater.* **34**, 2410676 (2024).
77. Tang, L. et al. Highly robust soft-rigid connections via mechanical interlocking for assembling ultra-stretchable displays. *npj Flex. Electron* **8**, 50 (2024).
78. Kim, M. et al. A gradient stiffness-programmed circuit board by spatially controlled phase-transition of supercooled hydrogel for stretchable electronics integration. *Adv. Mater.* **36**, 2313344 (2024).

Acknowledgements

This study was supported by the Japan Society for the Promotion of Science (JSPS) KAKENHI Grant-in-Aid for Transformative Research Areas (No. 24H00890), a Grant-in-Aid for Scientific Research A (No. 20H00213), a Grant-in-Aid for Challenging Research (No. 22K18288) and the Japan Agency for Medical Research and Development (AMED) under Grant (No. 23hm0102085h0004).

Author contributions

Y.S., N.F. and S.S. conceptualized the study and performed data collection. Y.I. and R.M. also contributed to the conceptualization. K.N. fabricated the device components and served as a research participant. N.N. fabricated and implemented the device components. T.T., I.Y. and N.N. developed the computer code. Y.I. and H.O. contributed to the critical review of the manuscript. T.S. provided conceptual advice for the study. T.U. and H.O. acquired the funding and served as the co-corresponding authors (jointly responsible for the work). All authors read and approved the final manuscript.

Competing interests

The authors declare no competing interests.

Additional information

Supplementary information The online version contains supplementary material available at https://doi.org/10.1038/s41528-026-00617-6.

Correspondence and requests for materials should be addressed to Takafumi Uemura or Hiroki Ota.

Reprints and permissions information is available at http://www.nature.com/reprints

Publisher's note Springer Nature remains neutral with regard to jurisdictional claims in published maps and institutional affiliations.

Open Access This article is licensed under a Creative Commons Attribution-NonCommercial-NoDerivatives 4.0 International License, which permits any non-commercial use, sharing, distribution and reproduction in any medium or format, as long as you give appropriate credit to the original author(s) and the source, provide a link to the Creative Commons licence, and indicate if you modified the licensed material. You do not have permission under this licence to share adapted material derived from this article or parts of it. The images or other third party material in this article are included in the article's Creative Commons licence, unless indicated otherwise in a credit line to the material. If material is not included in the article's Creative Commons licence and your intended use is not permitted by statutory regulation or exceeds the permitted use, you will need to obtain permission directly from the copyright holder. To view a copy of this licence, visit http://creativecommons.org/licenses/by-nc-nd/4.0/.

© The Author(s) 2026